

B-Site Doping Boosts the OER and ORR Performance of Double Perovskite Oxide as Air Cathode for Zinc-Air Batteries

Cagla Ozgur,^[a] Tuncay Erdil,^[a] Uygar Geyikci,^[a] Ilker Yildiz,^[b] Ersu Lokcu,^[c] and Cigdem Toparli^{*[a]}

Double perovskite oxides are key players as oxygen evolution and oxygen reduction catalysts in alkaline media due to their tailorabile electronic structures by doping. In this study, we synthesized B-site doped $\text{NdBaCo}_a\text{Fe}_{2-a}\text{O}_{5+\delta}$ ($a=1.0, 1.4, 1.6, 1.8$) electrocatalysts, systematically probed their bifunctionality and assessed their performance in zinc-air batteries as air cathodes. X-ray photoelectron spectroscopy analysis reveals a correlation between iron reduction and increased oxygen vacancy content, influencing electrocatalyst bifunctionality by lowering the work function. The electrocatalyst with highest cobalt content, $\text{NdBaCo}_{1.8}\text{Fe}_{0.2}\text{O}_{5+\delta}$ exhibited a bifunctionality value of 0.95 V,

outperforming other synthesized electrocatalysts. Remarkably, $\text{NdBaCo}_{1.8}\text{Fe}_{0.2}\text{O}_{5+\delta}$ demonstrated facilitated charge transfer rate in oxygen evolution reaction with four-electron oxygen reduction reaction process. As an air cathode in a zinc-air battery, $\text{NdBaCo}_{1.8}\text{Fe}_{0.2}\text{O}_{5+\delta}$ demonstrated superior performance characteristics, including maximum capacity of 428.27 mA h at 10 mA cm^{-2} discharge current density, highest peak power density of 64 mW cm^{-2} , with an enhanced durability and stability. It exhibits lowest voltage gap change between charge and discharge even after 350 hours of cyclic operation with a rate capability of 87.14%.

Introduction

Renewable energy sources such as solar, and wind have emerged as the most promising alternatives to conventional fossil fuels. Nonetheless, a fundamental challenge lies in the effective storage of the energy harnessed from these sources within power generation facilities. Therefore, it is crucial to develop cutting-edge energy storage systems that are reliable, efficient, and extremely safe. Due to their substantial theoretical specific energy densities, cost-effectiveness, and safety characteristics, zinc-air batteries (ZABs) have garnered considerable interest within the spectrum of energy storage devices as a prospective and sustainable electrochemical energy storage solution for the future.^[1–4] The practical viability of ZABs requires an economically feasible, highly efficient, and chemically stable catalyst for both the oxygen evolution reaction (OER) and the oxygen reduction reaction (ORR) occurring at the air

electrode.^[5–7] In the contemporary landscape, state-of-the-art electrocatalysts like IrO_2 , Pt/C, and RuO_2 find application in these batteries to expedite these reactions. Despite their elevated bifunctional activity of these electrocatalysts for both OER/ORR, their high cost and scarcity reduces the enhancement of ZABs toward commercial viability.^[8–10] Hence, it is crucial to design enduring, effective, and economically viable bifunctional electrocatalysts for OER and ORR, to be employed in the air cathode of rechargeable ZABs.^[11,12]

Double perovskite oxides (designated as $\text{A}_2\text{BB}'\text{O}_6$) display enhanced stability and superior electrocatalytic performance when compared to their single perovskite oxide counterparts.^[13–17] These compounds possess two distinct octahedral sites, designated as BO_6 and $\text{B}'\text{O}_6$, comprised of alternating pairs of B and B' atoms bound to oxygen. The disposition of cations within the B-site, along with the oxidation state of the transition metal, emerge as the primary factors governing the electrocatalytic efficacy of double perovskite oxide catalysts.^[18] In that context, metal-oxygen covalency, hybridization of metal M 3d and oxygen O 2p, plays a critical role on the electrocatalytic performance of these materials.^[19–23] Furthermore, perovskite oxide structure with a structured network of oxygen vacancies can improve the transport of oxygen ions and conductivity, which can enhance the kinetics of both OER and ORR.^[24–27] Therefore, several approaches have been employed to tailor the surface electronic structure and increase the number of active sites for electrochemical reactions.^[28–31] One of the simple and fast method to adjust electronic characteristics of perovskite oxide is a doping strategy.^[32–37] For instances, doping divalent Sr^{2+} cations into LaCoO_3 at the A-site significantly enhances its electrocatalytic activity by increasing the concentration of oxygen vacancies and promoting higher

[a] C. Ozgur, T. Erdil, U. Geyikci, C. Toparli
Department of Metallurgical and Materials Engineering, Middle East Technical University, Ankara 06800, Turkey
E-mail: ctoparli@metu.edu.tr

[b] I. Yildiz
Central Laboratory Middle East Technical University, Ankara 06800, Turkey

[c] E. Lokcu
Department of Metallurgical and Materials Engineering, Eskisehir Osmangazi University, Eskisehir 26040, Turkey

Supporting information for this article is available on the WWW under <https://doi.org/10.1002/cphc.202400531>

© 2024 The Authors. ChemPhysChem published by Wiley-VCH GmbH. This is an open access article under the terms of the Creative Commons Attribution License, which permits use, distribution and reproduction in any medium, provided the original work is properly cited.

oxidation states of B-site Co cations, thereby improving Co 3d–O 2p hybridization.^[38] Similarly, doping Co into LaMn_{1-x}Co_xO₃ at the B-site enhances OER performance by promoting the conversion of OOH⁻ to O₂ via mixed Mn⁴⁺/Mn³⁺ oxidation states.^[39] In other study, Kim et al. reported that doping transition-metal oxides such as Fe²⁺, Ni²⁺, Cu²⁺, and Mn²⁺ into the B-sites of NdBa_{0.75}Ca_{0.25}Co₂O_{5+δ} catalyst enhances electron and oxygen-ion mobility by promoting the formation of oxygen vacancies in double perovskite oxides.^[40] Moreover, researches shows us that doping both A and the B-site can enhance the bifunctional activity. For example, perovskite oxides with Ba and Sr occupying the A site demonstrate fast ion transport kinetics, whereas compositions rich in Co at the B-site exhibit higher kinetic coefficients compared to those rich in Fe.^[41] Merkle et al. reported that incorporating cobalt into Ba_{0.5}Sr_{0.5}Co_{1-y}Fe_yO_{3-y} reduces the energy required for O-vacancy formation, thanks to the proximity of electronic states' density to the Fermi level. This proximity makes it easier to reduce Co⁴⁺ to Co³⁺ compared to Fe⁴⁺ to Fe³⁺.^[42]

Here, we formulated electrocatalysts by introducing B-site doping into double perovskite oxide structures, specifically for utilization in rechargeable ZABs. We successfully synthesized a series of NdBaCo_aFe_{2-a}O_{5+δ} (NBCF) compounds, where 'a' assumes values of 1.0, 1.4, 1.6, and 1.8 denoted as NBCF double perovskite oxides. Through systematic investigation, we proceed to compare their bifunctional electrocatalytic performance in OER/ORR, elucidating the influence of varying cobalt and iron content on the electrocatalytic activity. Electrocatalysts denoted as NdBaCo_aFe_{2-a}O_{5+δ} (with 'a' value of 1.0, 1.4, 1.6, and 1.8) were synthesized using the modified sol-gel Pechini method and subsequently subjected to calcination. Following this thermal treatment, comprehensive material characterization encompass-

ing X-Ray diffraction (XRD), scanning electron microscopy (SEM), X-Ray photoelectron spectroscopy (XPS) and ultraviolet photo-electron spectroscopy (UPS) was performed. The bifunctional electrocatalytic performance in OER and ORR of these electrocatalysts was assessed via rotating disc electrode (RDE) setup, employing cyclic voltammetry (CV), linear sweep voltammetry (LSV), and electrochemical impedance spectroscopy (EIS) methodologies for comparative analysis. Ultimately, the electrocatalysts were incorporated into ZAB as air electrode. Electro-catalyst with lowest iron content, NdBaCo_{1.8}Fe_{0.2}O_{5+δ}, at the air cathode led to notable improvements in the ZAB's performance. Notably, the ZAB featuring the NdBaCo_aFe_{2-a}O_{5+δ} electro-catalyst exhibited an improved maximum capacity of 428.27 mAh at 10 mA cm⁻², superior peak power density of 64 mW cm⁻², exceptional durability, and stability even over a span of 350 hours of cyclic charge-discharge.

Results and Discussion

Characterization of the Crystal Structure

The crystal structure of the NBCF double perovskite oxides was examined through XRD. Figure 1 provides a visualization of the XRD patterns alongside the outcomes of the Rietveld refinement analysis. The XRD patterns distinctly indicate that all the NBCF double perovskite oxides exhibit a single phase. Remarkably, no distinctive peaks corresponding to the oxides, hydroxides of Nd, Ba, Co, Fe, or impurities were detected. Furthermore, the structural characteristics, including the space groups and crystal structure of the NBCFs, were determined using the Rietveld Refinement methodology. The results revealed that

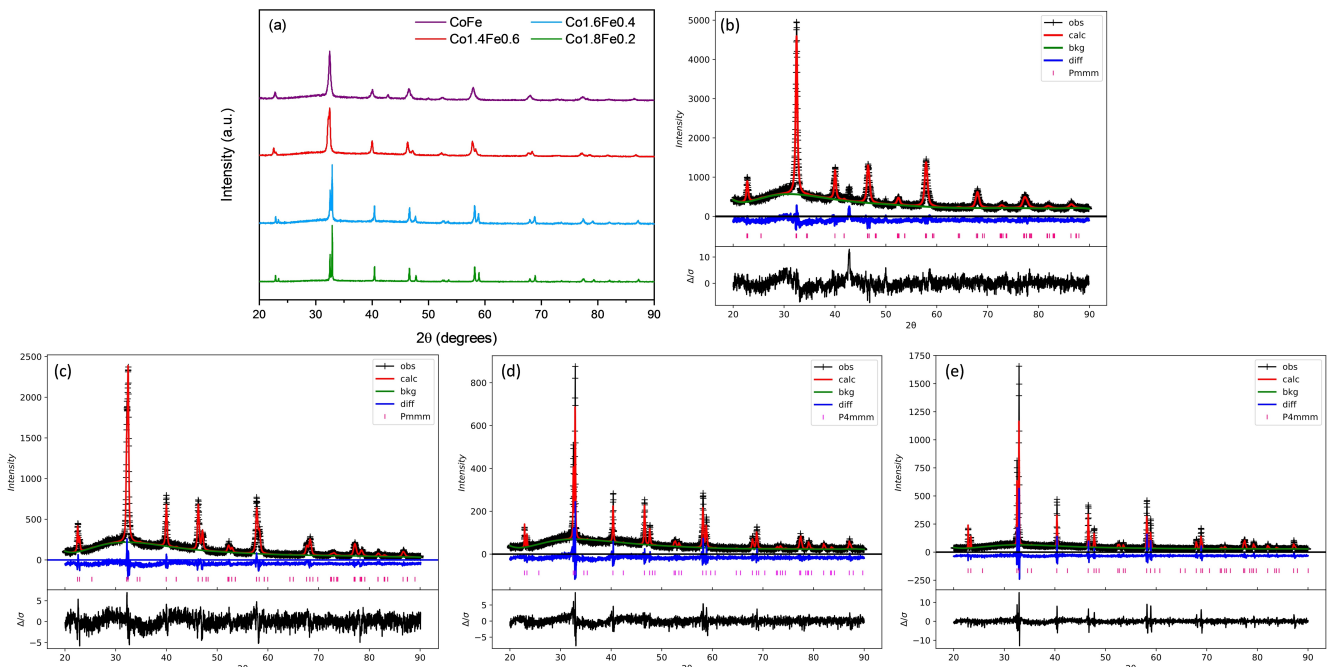


Figure 1. (a) XRD patterns of NBCF double perovskite oxides. Rietveld refinement analysis for the XRD of (b) NdBaCoFeO_{5+δ} (CoFe) (c) NdBaCo_{1.4}Fe_{0.6}O_{5+δ} (Co1.4Fe0.6) (d) NdBaCo_{1.6}Fe_{0.4}O_{5+δ} (Co1.6Fe0.4) (e) NdBaCo_{1.8}Fe_{0.2}O_{5+δ} (Co1.8Fe0.2).

Table 1. Lattice parameters, crystal volume, crystal structure and space group for CoFe, Co1.4Fe0.6, Co1.6Fe0.4 and Co1.8Fe0.2.

	a	b	c	Crystal volume	Crystal structure	Space group
NdBaCoFeO _{5+δ} (CoFe)	3.90908	3.90284	7.76516	118.47	Orthorhombic	Pmmm
NdBaCo _{1.4} Fe _{0.6} O _{5+δ} (Co1.4Fe0.6)	3.90752	3.90533	7.68501	117.27	Orthorhombic	Pmmm
NdBaCo _{1.6} Fe _{0.4} O _{5+δ} (Co1.6Fe0.4)	3.90198	3.90198	7.64396	116.38	Tetragonal	P4/mmm
NdBaCo _{1.8} Fe _{0.2} O _{5+δ} (Co1.8Fe0.2)	3.90304	3.90304	7.62614	116.17	Tetragonal	P4/mmm

CoFe and Co1.4Fe0.6 exhibit an orthorhombic crystal structure, with a designated space group of "Pmmm." Upon an increase in cobalt content alongside a decrease in iron content, the crystal structure transitions to a tetragonal configuration, aligning with the space group "P4/mmm." Lattice parameters and total crystal volumes for the NBCF double perovskite oxides are provided in Table 1. Notably, CoFe displays greater lattice parameters and a correspondingly larger crystal volume of 118.47 Å³, whereas Co1.8Fe0.2 exhibits comparatively smaller lattice parameters and a crystal volume of 116.17 Å³. The presence of larger iron ionic size led to a more pronounced lattice distortion, resulting in increased total volume when the double perovskite oxide has higher iron content.

We conducted a morphological examination of the synthesized NBCF double perovskite oxides with SEM, as depicted in Figure 2. The SEM images revealed particles at the submicron scale, typically measuring several hundred nanometers. While there was some variation in the shape and size of these particles, there was overall consistency in terms of particle size

and shape across all the perovskite oxides. This suggests that any potential impact of particle size and morphology on electrocatalytic activity can be considered minimal. To gain insights into the elemental distribution within the double perovskite oxides, we employed energy-dispersive X-ray (EDX) mapping. The EDX mapping results for NBCF double perovskite oxides, illustrated in Figure 2, indicated a uniform distribution of all elements, including Nd, Ba, Co, Fe, and O, throughout the particles.

XPS was employed to analyze the surface chemical composition and chemical states of the elements presented in the NBCF electrocatalysts. Figure 3 shows the XPS core level spectra of Fe 2p, and Co 2p. In Figure 3a,c, Fe (III) 2p_{3/2} satellite can be clearly seen which exhibit Fe₂O₃. Hence, for CoFe and Co1.4Fe0.6 iron is present in both Fe⁺² and Fe⁺³ oxidation states in the structure.^[43] However, for Co1.6Fe0.4 and Co1.8Fe0.2 Fe (II) 2p_{3/2} satellite which implies FeO appears in the Fe 2p XPS spectra (Figure 3e,g).^[44] Hence, as the iron amount in the NBCF double perovskite oxide decreases, the oxidation state of iron decreases to Fe⁺². In Figure 3(b,d,f,h) Co 2p spectra (Co 2p_{3/2}, and Co 2p_{1/2}, peaks located at 780 eV, and 796 eV binding energies respectively) exhibit Co₃O₄, implying all the samples have the same state of Co.

Figure 4 shows the fitted O 1s XPS spectra for NBCF electrocatalysts. Fitted O 1s XPS spectra exhibits the oxygen vacancy, and lattice oxygen at binding energies of 531 eV, and 529 eV respectively. Oxygen vacancy peak accounts for 46.57, 58.40, 59.78, and 57.65 % of the overall O 1s XPS spectra peak area, whereas the lattice oxygen peak constitutes 37.45, 26.37, 23.34 and 27.51% of the total area for CoFe, Co1.4Fe0.6, Co1.6Fe0.4 and Co1.8Fe0.2 respectively. Hence, as the cobalt amount in the NBCF double perovskite oxide increases the oxidation state of iron transitions from +3 to +2, whereas the oxidation state of cobalt remains unchanged. Consequently, there is an escalation in the concentration of oxygen vacancies within the structure.

Electrochemical Characterization of the Electrocatalysts

To comprehend the electrocatalytic efficiency of NBCF electrocatalysts, a RDE in conjunction with a standard three-electrode system was employed. LSV tests were conducted employing an Ag/AgCl reference electrode, and the subsequently recorded potentials were then converted to the reference RHE scale. The geometric area of the glassy carbon electrode, measured at 0.0707 cm², was used to normalize the LSV profiles (Figure 5a).

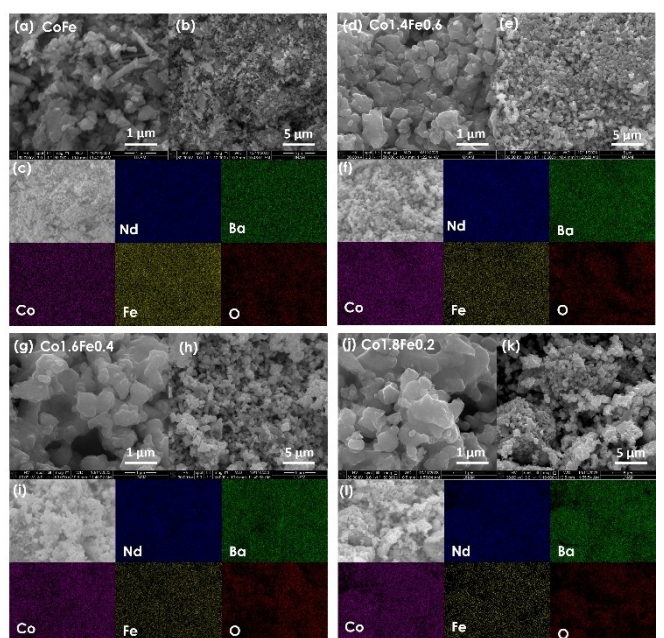


Figure 2. CoFe's (a) SEM images at 50000x magnification (b) SEM images at 10000x mag. (c) EDS Mapping of Nd, Ba, Co, Fe, and O. Co1.4Fe0.6's (d) SEM images at 50000x magnification (e) SEM images at 10000x mag. (f) EDS Mapping of Nd, Ba, Co, Fe, and O. Co1.6Fe0.4's (g) SEM images at 50000x magnification (h) SEM images at 10000x mag. (i) EDS Mapping of Nd, Ba, Co, Fe, and O. Co1.8Fe0.2's (j) SEM images at 50000x magnification (k) SEM images at 10000x mag. (l) EDS Mapping of Nd, Ba, Co, Fe, and O.

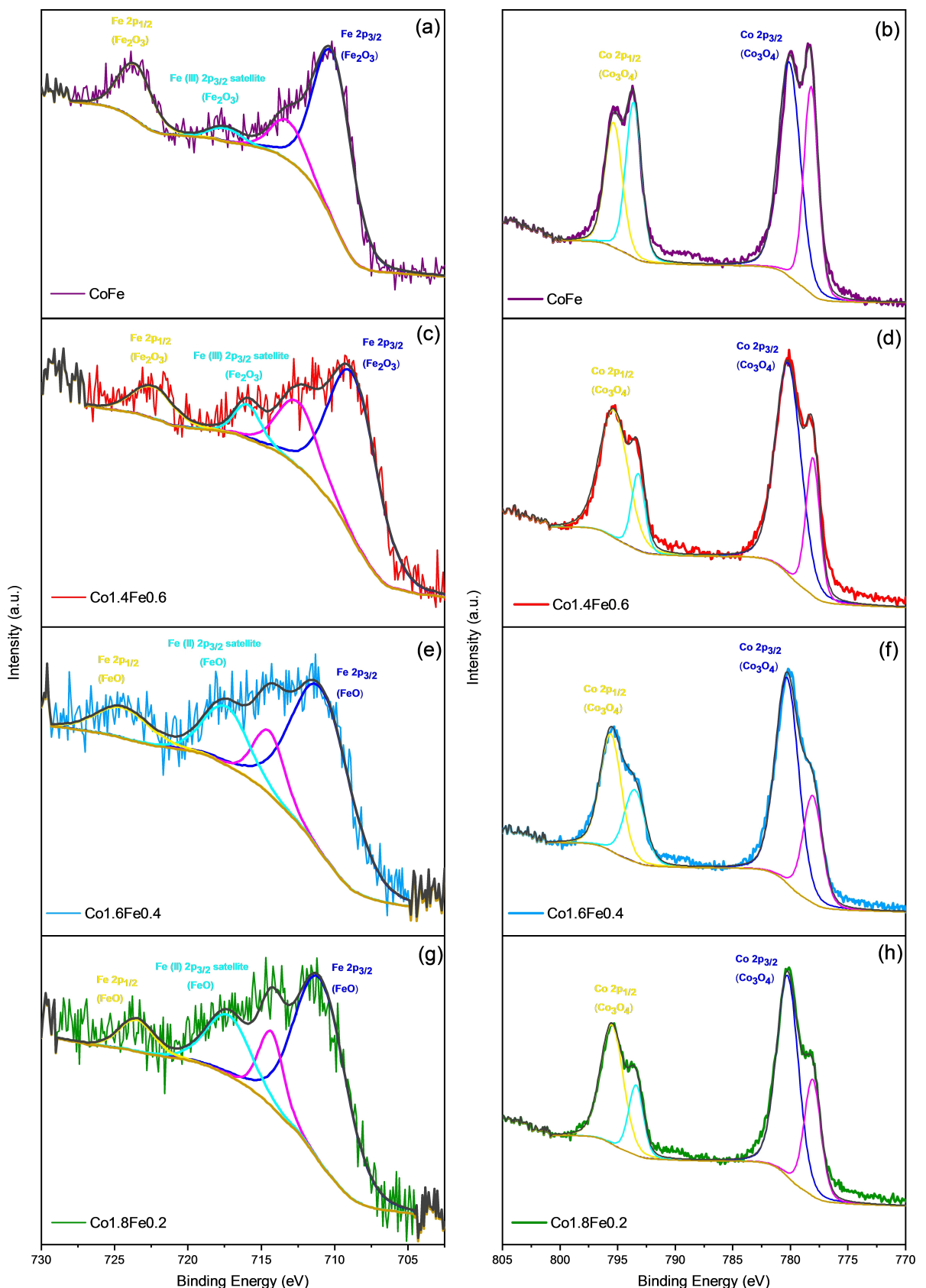


Figure 3. XPS survey spectra of Fe 2p and Co2p respectively for (a,b) CoFe (c,d) Co1.4Fe0.6 (e,f) Co1.6Fe0.4 (g,h) Co1.8Fe0.2.

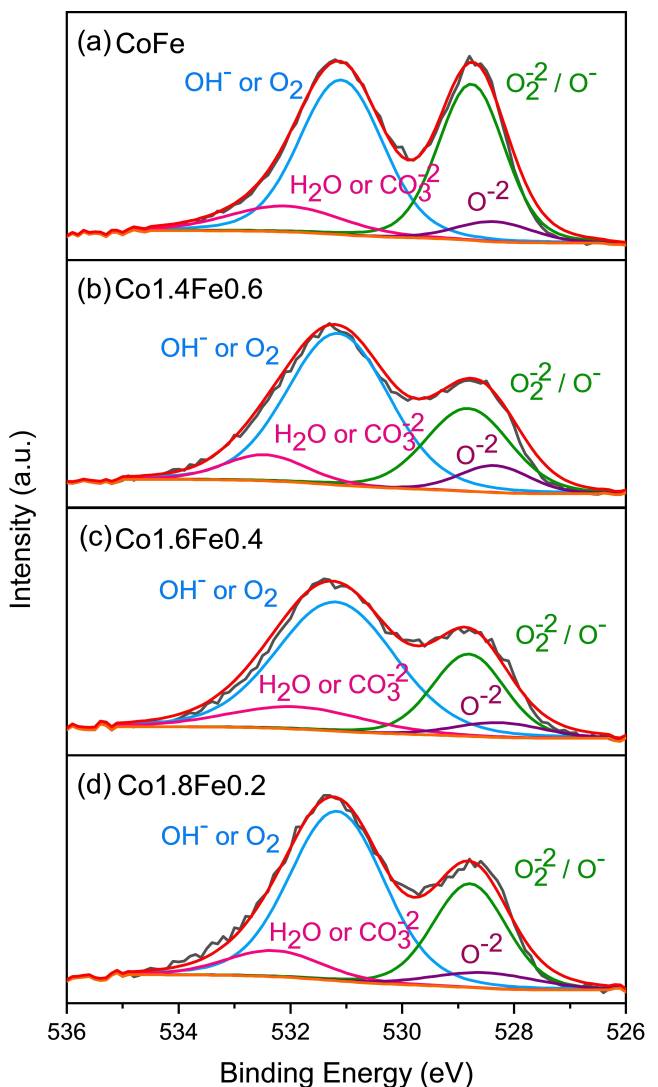


Figure 4. XPS O 1s spectra for (a) CoFe (b) Co1.4Fe0.6 (c) Co1.6Fe0.4 (d) Co1.8Fe0.2.

Notably, overpotential values of the NBCF electrocatalysts were evaluated at a current density of 10 mA cm^{-2} , a fundamental limit for comprehending a catalyst's electrocatalytic activity as established in the literature. As a result of this investigation, the determined overpotential values for the NBCF electrocatalysts are as follows: 439 mV for CoFe, 384 mV for Co1.4Fe0.6, 428 mV for Co1.6Fe0.4, and 444 mV for Co1.8Fe0.2. Consequently, it is evident that Co1.4Fe0.6 showcases the lowest overpotential within the spectrum of the NBCF electrocatalysts. Moreover, these overpotential values for the NBCF electrocatalysts exhibit comparability with those of benchmark electrocatalysts, namely IrO_2 , RuO_2 ($\approx 300\text{--}450$ mV in 0.1 M KOH), and Pt/C that have been previously reported in the literature.^[8,45–47] Furthermore, Tafel plots were derived to facilitate a comparative assessment of the reaction kinetics inherent in the NBCF electrocatalysts, as depicted in Figure 5b. Tafel slopes are 106 mV dec^{-1} for CoFe, 83 mV dec^{-1} for Co1.4Fe0.6, 86 mV dec^{-1} for Co1.6Fe0.4, and 96 mV dec^{-1} for Co1.8Fe0.2. Despite Co1.4Fe0.6 displaying a

diminished Tafel slope, signifying accelerated reaction kinetics, it is noteworthy that the Tafel slopes across the spectrum of NBCF electrocatalysts are closely aligned, indicating a high degree of similarity in their reaction kinetics. Then, the charge transfer rate of the NBCF electrocatalysts was assessed through the utilization of EIS. The EIS findings distinctly indicate that the conductivity of the Co1.8Fe0.2 electrocatalyst surpasses that of the other NBCF double perovskite oxide electrocatalysts (Figure 5c). This enhanced conductivity exhibited by the Co1.8Fe0.2 electrocatalyst highlights its enhanced ability for charge transfer during the OER. Although the slightly elevated overpotential observed for the Co1.8Fe0.2 electrocatalyst in comparison to the other NBCF counterparts, its charge transfer rate remains prominent feature. Furthermore, electrochemically active surface area (ECSA) of the NBCF electrocatalysts was determined using the double layer capacitance (C_{dl}), as portrayed in Figure 5d. The calculated C_{dl} values for CoFe, Co1.4Fe0.6, Co1.6Fe0.4, and Co1.8Fe0.2 were determined as 4.01, 9.04, 14.06, and 8.93 mF cm^{-2} , respectively. This analysis establishes that Co1.6Fe0.4 betters the other electrocatalysts in terms of ECSA, signifying its larger electrochemically active surface area. ECSA analysis indicates that the heightened electrocatalytic performance of Co1.4Fe0.6 does not stem from its electrochemically active surface area; rather, it may be attributed to its intrinsic activity. Lastly, for a comprehensive grasp of the intrinsic activity of the electrocatalysts, the mass activity (MA) and specific activity (SA) were evaluated (Figure 5e). The electrocatalysts' mass loading was employed to compute the mass activity, whereas the specific activity was determined utilizing the ECSA. Remarkably, Co1.4Fe0.6 emerged as notably superior to the other electrocatalysts in terms mass activity and specific activity. Specifically, MA and SA of Co1.4Fe0.6 were quantified at 33.53 A g^{-1} and 0.318 mA cm^{-2} , respectively, outperforming the benchmark electrocatalyst RuO_2 's corresponding MA (8.87 A g^{-1}) and SA ($0.06224 \text{ mA cm}^{-2}$).^[48] This demonstrates the improved intrinsic activity exhibited by Co1.4Fe0.6. Figure 5f displays Mott-Schottky plots for NBCF electrocatalyst. All the electrocatalysts demonstrate p-type behavior, as evidenced by the negative slope observed after 1.2 V vs RHE, which corresponds to the working range of the oxygen evolution reaction at 1.23 V vs RHE. Notably, there is no transition from n-type to p-type semiconductor behavior in the potential range between 1.2 V and 1.7 V. The determination of the flat-band potential (E_{fb}) relies on linear extrapolation within the p-type behavior region. A more positively shifted flat-band potential indicates a greater restriction on electrocatalytic OER activity.^[49,50] Among the NBCF double perovskite oxide electrocatalysts, Co1.4Fe0.6 exhibits low E_{fb} at 1.53 V vs. RHE, aligning with its overpotential value of 384 mV. Co1.4Fe0.6 demonstrates superior OER electrocatalytic activity with the lowest flat-band potential. Consequently, it can be deduced that Co1.4Fe0.6 holds potential as a promising candidate for an OER electrocatalyst, attributable to its lower overpotential and enhanced intrinsic activity. Conversely, the Co1.8Fe0.2 electrocatalyst exhibits higher charge transfer rate, accompanied by an overpotential and ECSA analogous to those of conventional OER electrocatalysts.

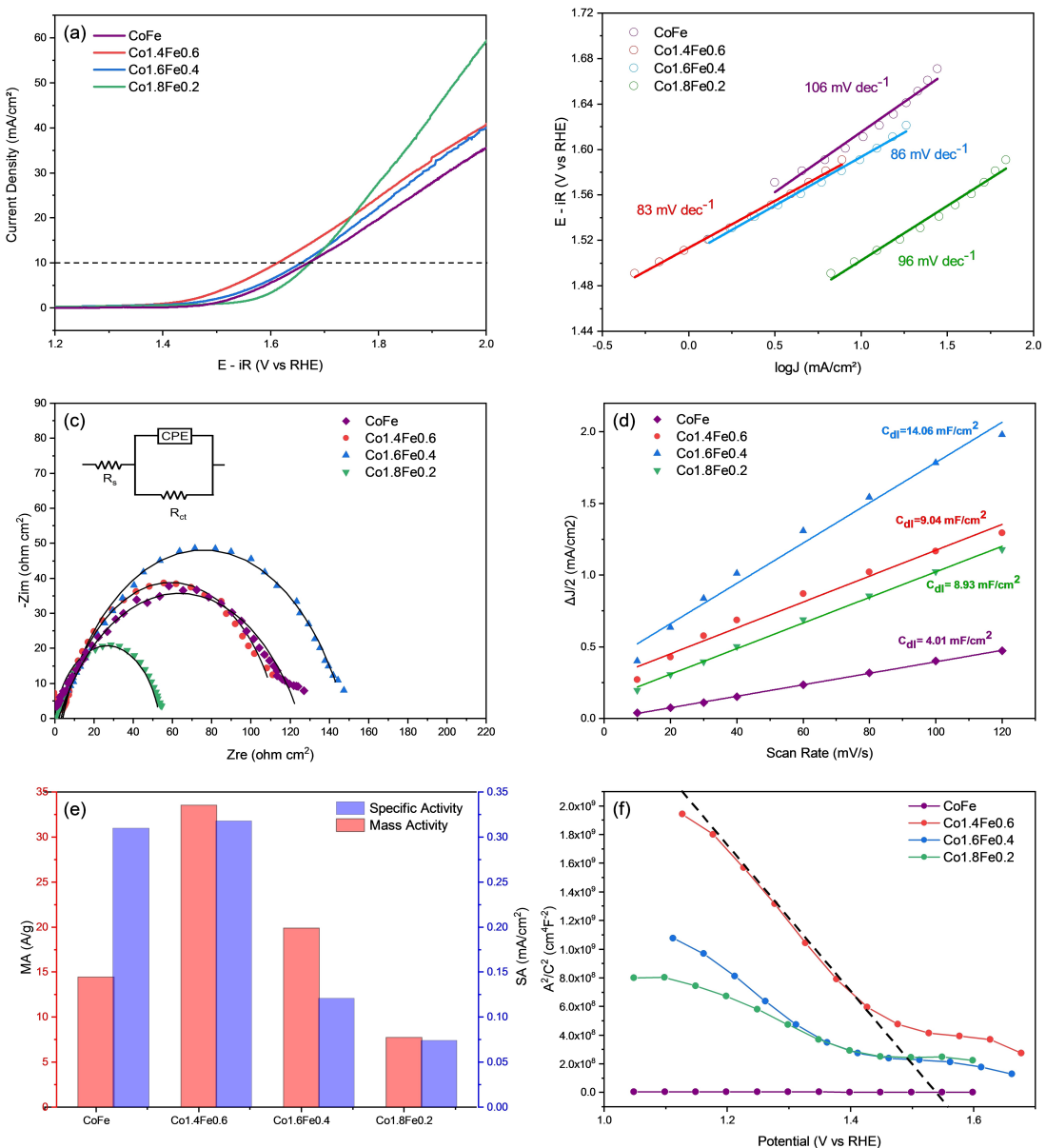


Figure 5. (a) LSV curves for OER activity (b) Tafel plots (c) EIS (d) Electric double layer capacitance (e) Mass activity and specific activity (f) Mott-Schottky plots for CoFe, Co1.4Fe0.6, Co1.6Fe0.4 and Co1.8Fe0.2.

Figure 6 illustrates the analysis of ORR activity for the NBCF double perovskite oxide electrocatalysts, aiming to identify the electrocatalysts' bifunctional OER/ORR performance. In a manner analogous to the approach adopted for OER activity assessment, LSV curves were obtained initially. Notably, the potentials recorded for CoFe, Co1.4Fe0.6, Co1.6Fe0.4, and Co1.8Fe0.2 stand at 0.52, 0.64, 0.65, and 0.73 V, respectively, corresponding to a current density of -1 mA cm^{-2} (Figure 5a). This affirms that Co1.8Fe0.2 boasts a superior ORR activity compared to the other NBCF electrocatalysts. Furthermore, the Tafel slopes, deduced from the Tafel plots, are determined as -179 , -234 , -328 , and -281 mV dec^{-1} for CoFe, Co1.4Fe0.6, Co1.6Fe0.4, and Co1.8Fe0.2, respectively (Figure 6b). Consequently, it can be deduced that the reaction kinetics of the Co1.8Fe0.2 electrocatalyst for ORR is comparable with those of

the other NBCF electrocatalysts. The Koutecky Levich (K-L) equation was utilized to determine the electron transfer number and kinetic current densities of the electrocatalysts. K-L plots were generated through performing LSV in a voltage range of 1.2 V to 0.14 V versus RHE at varying rotation speeds (800, 1200, 1600, 2000 rpm (Figure S1), employing a scan rate of 5 mV s^{-1} . As the rotational speed of the working electrode increased, a corresponding elevation in the reduction current was observed, attributed to enhanced mass transport at the working electrode's surface. The higher rpm facilitated improved oxygen diffusion from the electrolyte to the electrocatalyst's surface. Notably, Co1.8Fe0.2 consistently exhibited a higher reduction current density at a constant potential and rotational speed. The K-L plots exhibited linearity, supporting the notion that the ORR follows first-order kinetics (Figure S2).

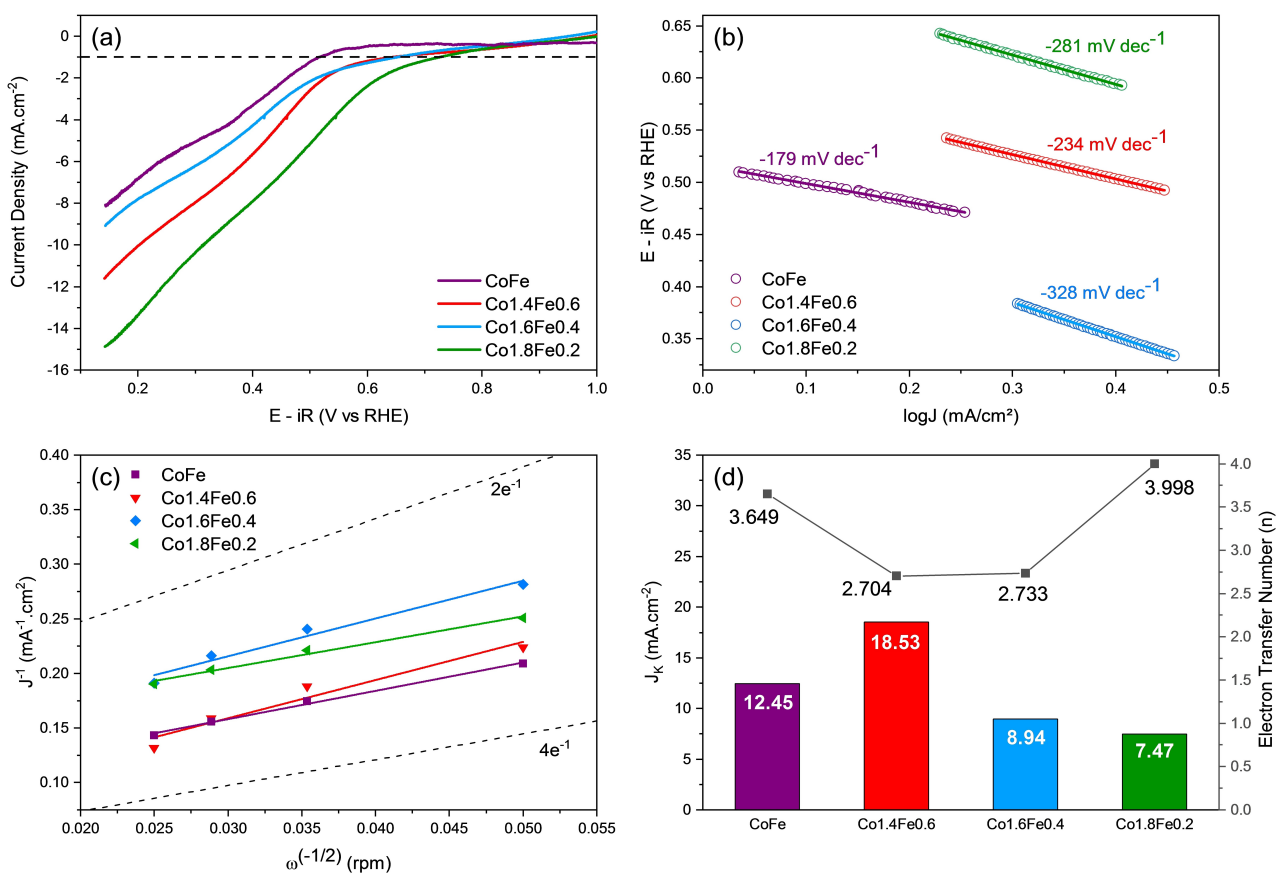


Figure 6. (a) LSV curves for ORR activity (b) Tafel plots (c) K-L plots (d) Electron transfer number (*n*) and kinetic current density (*J_k*) for CoFe, Co1.4Fe0.6, Co1.6Fe0.4 and Co1.8Fe0.2.

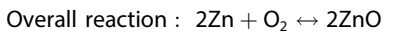
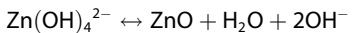
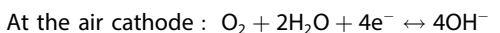
At a low voltage of 0.15 V versus RHE, the electron transfer number (*n*) was determined to be 3.649, 2.704, 2.733, and 3.998 for CoFe, Co1.4Fe0.6, Co1.6Fe0.4, and Co1.8Fe0.2, respectively (Figure 6d). Considering that the electron transfer number for Co1.8Fe0.2 is closer to 4, it can be inferred that the 4-electron ORR process predominates in Co1.8Fe0.2.^[51,52]

In conclusion, to comprehend the bifunctional OER/ORR electrocatalytic activity the potential gap between current densities of -1 mA cm^{-2} and 10 mA cm^{-2} was used to calculate the bifunctionality (BI) value. The BI parameter provides insight into the catalyst's elevated OER/ORR electrocatalytic activity within an alkaline environment. In this study, the BI values stand at 1.15, 0.97, 1.01, and 0.95 V for CoFe, Co1.4Fe0.6, Co1.6Fe0.4, and Co1.8Fe0.2, respectively. Consequently, among the NBCF double perovskite oxide electrocatalysts, Co1.8Fe0.2 demonstrates enhanced bifunctional OER/ORR electrocatalytic activity characterized by a low BI value.

Zn-Air Battery Performance Evaluation

Rechargeable ZABs were assembled utilizing a zinc plate as the anode, NBCF double perovskite oxides as the air cathodes, and an electrolyte consisting of 6 M KOH with an additive of 0.2 M Zn(OAc)₂. In rechargeable ZABs, the air cathode plays a pivotal

role in both the charging process involving OER and the discharging process involving ORR. The overall reactions occurring within the ZABs are represented as follows:



The polarization curves illustrating the charge and discharge characteristics of the ZAB utilizing NBCF cathodes are presented in the Figure 7a. The Co1.8Fe0.2-based ZAB necessitates 2.086 V and 1.069 V during the charging and discharging respectively, to attain a current density of 10 mA cm^{-2} . Conversely, other NBCF-based ZABs exhibit larger voltage differentials, notably equimolar CoFe displaying the most substantial difference between discharging and charging, as depicted in the Figure 7a. This phenomenon indicates a minimal distinction between charge and discharge processes, underscoring the favorable compatibility of the Co1.8Fe0.2 double perovskite oxide electrocatalyst with both OER and ORR. Moreover, the Co1.8Fe0.2-based ZAB demonstrates the highest and notable

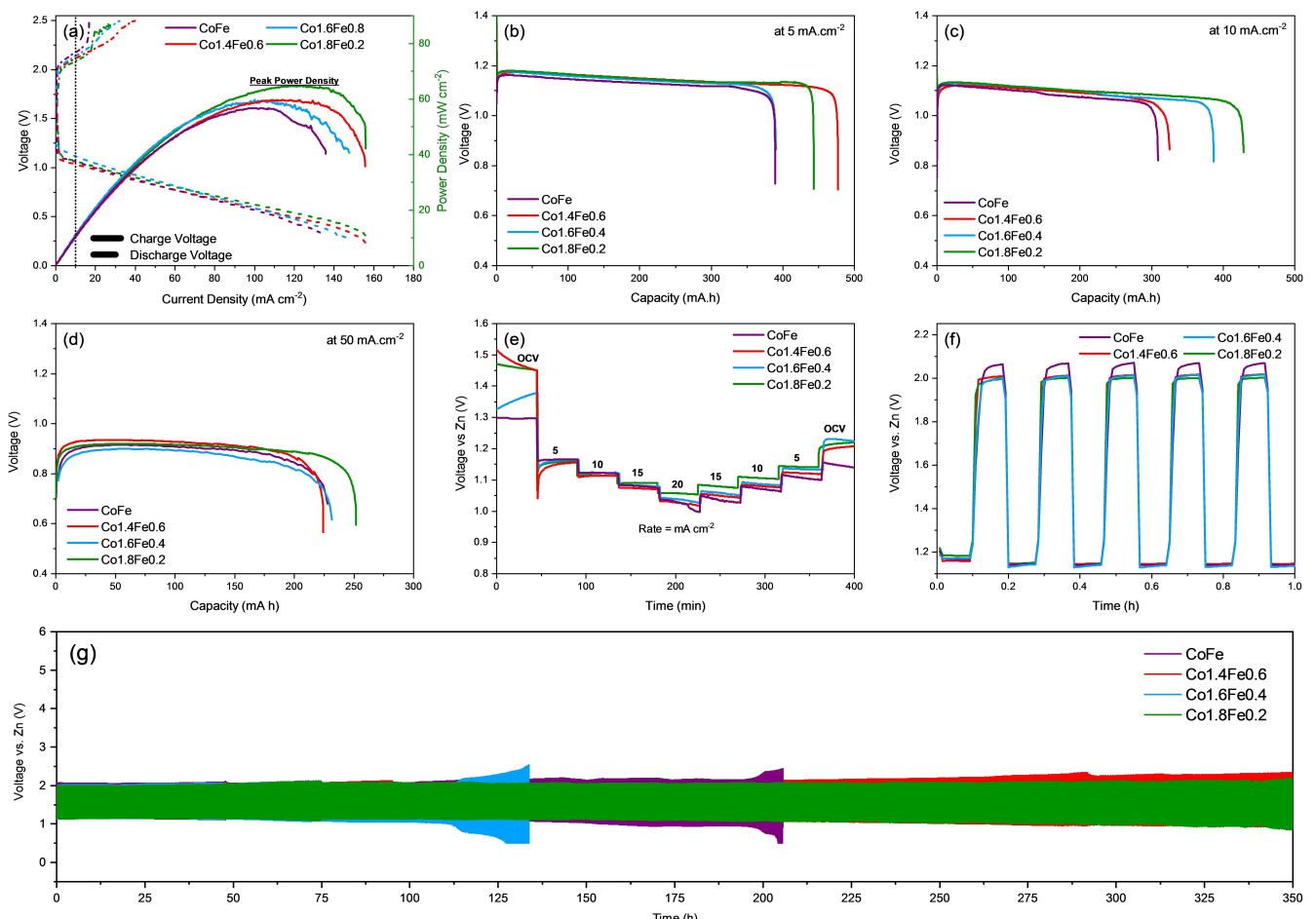


Figure 7. ZABs with NBCF-based air cathodes' (a) Peak power density plots with charge and discharge polarization curves (b) Capacities at 5 mA cm^{-2} (c) Capacities at 10 mA cm^{-2} (d) Capacities at 50 mA cm^{-2} (e) Rate capability from 0 to 20 then 0 mA cm^{-2} (f) Durability performance in the first hour of cyclic charge-discharge (g) Cyclic charge-discharge at 5 mA cm^{-2} .

peak power density, reaching 64 mW cm^{-2} at a higher current density of 135 mA cm^{-2} . In contrast, the second-best peak power density is observed in the Co1.4Fe0.6-based ZAB at 59 mW cm^{-2} but at a lower current density of 120 mA cm^{-2} . Equimolar CoFe exhibits the smallest peak power density, observed at the lowest current density of 100 mA cm^{-2} .

Figure 7b,c and Figure 7d presents the discharge capacities of NBCF-based ZAB under 5 mA cm^{-2} , 10 mA cm^{-2} , and 50 mA cm^{-2} current densities respectively. Notably, the ZABs exhibit higher capacities at 5 mA cm^{-2} compared to 10 mA cm^{-2} and 50 mA cm^{-2} . Specifically, the Co1.8Fe0.2 achieves a capacity of 443.34 mAh at 5 mA cm^{-2} , 428.27 mAh at 10 mA cm^{-2} , and 251.74 mAh at 50 mA cm^{-2} . This suggests that Co1.8Fe0.2 demonstrates a stable capacity across different current densities, with its capacity retention being less influenced by increasing current density. In contrast, the Co1.4Fe0.6-based ZAB shows a strong dependence on current density, with the highest capacity of 477.28 mAh at 5 mA cm^{-2} , the second-lowest capacity of 324.59 mAh at 10 mA cm^{-2} and lowest capacity of 225.18 mAh at 50 mA cm^{-2} among the other NBCF-based ZABs. This indicates that the capacity of Co1.4Fe0.6-based ZAB may not be sustained at higher current densities,

while Co1.8Fe0.2 maintains the capacity that is not significantly lower even at higher current densities. Consequently, Co1.8Fe0.2 exhibits greater stability, making it a more reliable battery than Co1.4Fe0.6, despite its slightly lower capacity change at lower current densities.

The rate capability and cyclic discharge stability of NBCF-based ZABs were evaluated by systematically varying the discharge rate from 0 to 20 mA cm^{-2} and subsequently returning to 0 mA cm^{-2} , while monitoring the output voltage (Figure 7d). The Co1.8Fe0.2-based ZAB exhibited exceptional rate capability and stability. Initially, the output voltage was 1.29 V , and after 400 minutes of operation, it decreased to 1.14 V , corresponding to 87.14% of the initial output voltage. Notably, this electrocatalyst displayed the lowest voltage retention after 400 minutes of continuous operation under various discharge current densities compared to other NBCF-based ZABs.

Furthermore, the cyclic charge-discharge performances of NBCF-based ZABs were assessed at a constant current density of 5 mA cm^{-2} at 5-minute intervals to understand their electrochemical durability under continuous charge-discharge conditions. Initially, the Co1.8Fe0.2-based ZAB exhibited charge and

discharge voltages of 1.98 V and 1.18 V, respectively, with a voltage gap of only 800 mV. In contrast, other NBCF-based ZABs, such as Co1.6Fe0.4, Co1.4Fe0.6, Co1.2Fe0.8, and CoFe, had voltage gaps of 822 mV, 846 mV, 840 mV, and 897 mV, respectively (Figure 7f). The Co1.8Fe0.2-based ZAB consistently demonstrated the smallest voltage gap. Over time, some NBCF-based ZABs experienced a loss of stability. The Co1.6Fe0.4-based ZAB lasted approximately 110 hours, Co1.2Fe0.8 lasted about 180 hours, and CoFe lasted about 200 hours before exhibiting a significant increase in their voltage gap. In contrast, the Co1.8Fe0.2 and Co1.4Fe0.6 batteries lasted more than 350 hours with a minimal increase in their voltage gap (Figure 7g). Even after this extended period, the voltage gap of the Co1.8Fe0.2 ZAB increased by only 41 % from the initial voltage gap after 350 hours, reaching 1.13 V. The voltage gap of the Co1.4Fe0.6-based ZAB increased to 1.37 V.

When comparing the performance of NBCF-based ZABs, it becomes evident that while some configurations outperform Co1.8Fe0.2 under specific conditions, overall, Co1.8Fe0.2-based ZAB exhibits the best rechargeable zinc-air battery performance. For instance, Co1.4Fe0.6 achieves the highest capacity at 5 mA cm^{-2} but experiences a decline in capacity at 10 mA cm^{-2} and 50 mA cm^{-2} , whereas Co1.8Fe0.2 maintains its capacity across different discharge currents. Co1.4Fe0.6 has a similar cyclic charge-discharge time as Co1.8Fe0.2 but demonstrates lower voltage stability. Additionally, its rate capability and peak power density are substantially lower than those of Co1.8Fe0.2-based ZAB. Despite CoFe-based ZAB showing a rate capability comparable to Co1.8Fe0.2, overall experimental results indicate that CoFe is the least effective cathode for rechargeable ZAB. Experimental data reveals that the electrocatalyst with the highest cobalt content, i.e., Co1.8Fe0.2, exhibits the highest peak power density (64 mW cm^{-2}), the highest capacity at 10 mA cm^{-2} discharge current density (428.27 mAh), a stable capacity retention, the highest rate capability (87.14%), and the longest cyclic charge-discharge time (350 hours), along with the lowest voltage gap after 350 hours. While the OER overpotential and Tafel slope of Co1.8Fe0.2 are moderate, its distinct advantages lie in its low resistivity and high charge transfer rate compared to other NBCF electrocatalysts. Notably, Co1.8Fe0.2 stands out in ORR performance, featuring the lowest onset potential, highest limiting current, low kinetic current density, and efficient ~4-electron transfer processes. The calculated electron transfer number for Co1.8Fe0.2 is 3.998, close to 4, indicating highly efficient ORR performance. The impact of ORR efficiency is evident in discharge-based experiments, such as peak power density, capacity measurements, and rate capability tests.

Analysis of the Electronic Structure

The work functions of NBCF electrocatalysts and UPS studies were performed by applying a bias voltage of -7 eV , the UPS spectra are shown in Figure 8a. The work function (ϕ) was calculated by subtracting the He (I) radiation (21.22 eV) from the high-binding-energy cut-off. The Fermi edge calibration was

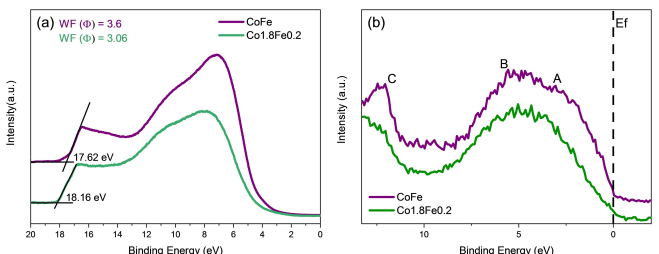


Figure 8. (a) UPS spectra (b) XPS valence band spectra of CoFe, and Co1.8Fe0.2.

performed with a sputter-cleaned Ag standard to ensure that all energies were referenced to a common Fermi level (0 eV). Thus, the work function was calculated using the following equation: $\phi = h_v - E_{\text{cut-off}}$, where h_v is the incident photoelectron energy (21.22 eV), $E_{\text{cut-off}}$ was determined from the linear extrapolation with the baseline of the secondary electron onset.^[53] The work function of Co1.8Fe0.2 is reduced to 3.06 eV from 3.6 eV for the CoFe, indicating the higher intrinsic conductivity of Co1.8Fe0.2 electrocatalyst which is compatible with the EIS results. The positioning of the O p-band center in relation to the Fermi energy (E_f) provided an alternative characterization of electrocatalytic performance. Thus, the valence band (VB) spectra of CoFe, and Co1.8Fe0.2 is shown in Figure 8b. VB spectrum shows us O 2p electronic states that are hybridized with Co 3d and Fe 3d derived states. Co 3d and Fe 3d states are marked as "A and B" in the 0–6 eV region, whereas O 2p character dominating in the 4–13 eV region farther from E_f marked as "C" in the XPS valence band spectra.^[54–56] XPS valence band spectra confirms that both Co1.8Fe0.2 and CoFe displays the hybridization of O 2p and Co/Fe 3d orbitals that reduces the charge transfer gap between the electrocatalyst surface and oxygen intermediate species (O_2^* , OH^* , O^* , OOH^*) in the alkaline electrolyte solution. This facilitates the exchange of $\text{O}_2^{2-}/\text{OH}^-$ on the surface for OH^- regeneration.^[20]

Materials Characterization after Battery Test

To understand the potential changes in the crystal structure of the Co1.8Fe0.2 electrocatalyst, XRD analysis was conducted following a 350-hour cyclic charge-discharge test. Figure 9 illustrates the XRD patterns of the Co1.8Fe0.2 double perovskite oxide both before and after the cyclic charge-discharge experiment. After the test, the XRD analysis of the Co1.8Fe0.2 air cathode reveals peaks indicative of a tetragonal structure, aligning with the space group "P4/mmm". Additionally, supplementary peaks corresponding to potassium oxide, potassium peroxide, and potassium hydroxide derivatives emerge in the XRD pattern, originating from the 6 M KOH electrolyte. Furthermore, the presence of zinc oxide peaks in the XRD pattern is attributed to the reduction of the Zn anode during the operation of the ZAB battery or the presence of Zn(OAc)_2 additive in the electrolyte. Consequently, it is concluded that

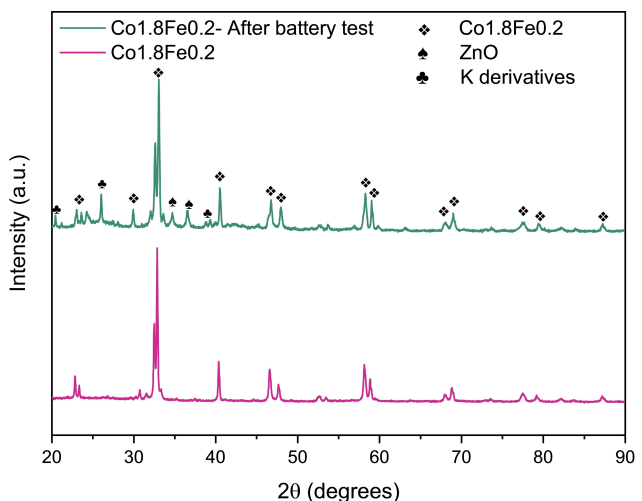


Figure 9. XRD patterns for Co1.8Fe0.2 before and after the cyclic charge-discharge ZAB experiment.

the crystal structure of Co1.8Fe0.2 remains stable even after 350 hours of cyclic charge-discharge testing.

Conclusions

Our results indicate that an increase in the Co content generates alterations in both the crystal and electronic structures, leading to an enhancement in bifunctional electrocatalytic performance. The crystal structure transformation from orthorhombic in CoFe to tetragonal in Co1.8Fe0.2 corresponds with the increase in Co content. Additionally, the oxidation state of iron transitions from +3 to +2, and the oxygen vacancy content rises with higher cobalt content. Notably, the increase in the oxygen vacancy content is correlated with the improved bifunctional electrocatalytic activity. Co1.8Fe0.2 exhibits the fastest charge transfer rate, optimal oxygen reduction reaction (ORR) performance with ~4 electron transfer number, and a noteworthy bifunctionality value of 0.95 V. In zinc-air batteries, the Co1.8Fe0.2-air cathode demonstrates remarkable performance, including a peak power density of 64 mW cm^{-2} , high capacity of 428.27 mAh at 10 mA cm^{-2} current density, and prolonged cyclic stability exceeding 350 hours at a constant 5 mA cm^{-2} charge-discharge current density with minimal increase in voltage gap. Comparative analysis with NBCF electrocatalysts reveals superior performance of the Co1.8Fe0.2-based zinc-air battery, characterized by enhanced capacity, durability, and efficiency related to its lower work function value of 3.06 eV. This investigation underscores the substantial impact of B-site cation ratios on oxygen vacancy generation, achieved by modulating the oxidation state of iron while maintaining cobalt's oxidation state. Our findings emphasize the potential for synthesizing NBCF with controlled cation ratios and oxygen vacancies, resulting in profound effects on bifunctional electrocatalytic performance and zinc-air battery efficiency.

Experimental Section

Fabrication of Double Perovskite Oxides

NdBaCo_aFe_{2-a}O_{5+δ} (where 'a' assumes values of 1.0, 1.4, 1.6, and 1.8), denoted as NBCF double perovskite oxides, were synthesized through a modified sol-gel Pechini method. Stoichiometric quantities of Nd(NO₃)₃·6H₂O (Sigma Aldrich), Ba(NO₃)₂ (Alfa Aesar 99%), Co(NO₃)₂·6H₂O (Alfa Aesar 98.9–102.0%), and Fe₃(NO₃)₃·9H₂O (Sigma Aldrich) were dissolved in deionized water and subjected to stirring on a hot plate at 100 °C. Subsequently, the solution was supplemented with citric acid and acrylamide as chelating agents. Following water evaporation, the resultant gel underwent drying at approximately 225 °C for approximately 24 hours, succeeded by calcination at 600 °C for 15 hours. At the final stage, the calcined powders were subjected to annealing at 1000 °C to obtain single phase material.

Materials Characterization

The crystal structure analysis of the samples was conducted through room temperature powder XRD employing Ni-filtered Cu K α radiation ($\lambda = 1.5406 \text{ \AA}$) within a 2θ range spanning 20° to 90°. Rietveld Refinement Method, facilitated by the EXPGUI interface and GSAS software was employed to refine the crystal structure. To investigate the microstructure and morphology of the synthesized NBCF powders, a Scanning Electron Microscope (FEI Nova Nano SEM 430) was utilized. For the computation of the specific surface areas of the NBCF double perovskite oxides, the Brunauer-Emmet-Teller (BET) methodology was employed within the context of a relative pressure range of $P/P_0 = 0.055$ to 0.30. The specific surface areas were determined through nitrogen (N₂) adsorption-desorption isotherms, using Quantachrome Corporation's Autosorb-6 apparatus. Prior to analysis, the samples underwent vacuum degassing at 300 °C for a duration of two hours. The chemical compositions of the NBCFs were examined using XPS facilitated by PHI 5000 Versa Probe spectrometer, employing Al K α radiation as the excitation source. All of the peaks were calibrated with a standard C 1s spectrum at 284.6 eV. UPS experiments carried out (Physical Electronics (PHI), Versa Probe 5000) under high vacuum with a base pressure of $1 \times 10^{-9} \text{ mbar}$. The He gas discharge lamp (21.22 eV) was used as the UV light source in UPS measurements.

Electrochemical Measurements

The electrochemical performance of NdBaCo_aFe_{2-a}O_{5+δ} (where 'a' is 1.0, 1.4, 1.6, and 1.8) double perovskite oxides was evaluated utilizing a RDE system (BASI) coupled with a GAMRY Reference 3000 potentiostat/galvanostat/ZRA. The experimental setup included a standard three-electrode cell, comprising an Ag/AgCl reference electrode, a platinum wire counter electrode, and a glassy carbon electrode (GCE) serving as the working electrode. The GCE was coated with a 10 μL catalyst ink, prepared by mixing 5 mg of Super-P carbon, 10 mg of NBCF powder, 200 μL of a 5 wt % Nafion solution (Sigma-Aldrich), and 2 mL of ethanol. Consequently, a mass loading of $0.15 \text{ mg}_{\text{HEO}} \cdot \text{cm}_{\text{disk}}^{-2}$ was achieved on the GCE. Prior to initiating the experiments, a 0.1 M potassium hydroxide (KOH, Alfa, 99.99%) electrolyte solution, unless specified otherwise, was saturated with oxygen for approximately 30 minutes. This standardized setup was consistently employed throughout the experimental procedures.

Throughout the experimental proceedings, a continuous supply of oxygen gas was maintained within the electrolyte to uphold the equilibrium between O₂ and H₂O at 1.23 V, while RDE operated at a fixed speed of 1600 rpm. Initially, a series of 10 CV cycles spanning

the potential range of 0.2 to 1.11 V vs Ag/AgCl was executed to activate the surface of the NBCF electrocatalysts. LSV tests were conducted within the potential window of 0.2 to 1.1 V vs Ag/AgCl, utilizing a scan rate of 10 mVs^{-1} to assess the OER activity. The potentials recorded were transformed to the reversible hydrogen electrode (RHE) scale using the Nernst Equation. During the evaluation of OER activity, gaseous evolved at the electrode surface is tried to sweep out from the surface by rotating the electrode. However, for precise evaluation scanning electrochemical microscopy (SCEM) can be used to calculate effective surface area.^[57,58] Tafel slopes were determined under steady-state conditions with the chronoamperometry (CA) technique within a potential range of 0.50 to 0.90 V versus Ag/AgCl, with 0.01 V increments. EIS measurements were conducted at 1.641 V vs. RHE. This assessment encompassed AC voltage with an amplitude of 10 mV, spanning a frequency range of 10^5 to 10^{-2} Hz .

The determination of the electrochemically active surface area (ECSA) of the electrocatalysts involved the utilization of double layer capacitance (C_{dl}), derived from CV analyses performed across distinct scan rates within the non-faradaic region. In an oxygen-saturated 1 M KOH solution, CVs were attained over a potential range between 0.2 and 0.3 V vs. Ag/AgCl at scan rates of 10, 20, 30, 40, 60, 80, 100, and 120 mVs^{-1} for NBCF electrocatalysts (Figure S3).^[59] A graph depicting scan rate against the reciprocal of the difference between anodic and cathodic current densities ($\Delta J/2 = (J_a - J_c)/2$) was then constructed at 0.25 V vs. Ag/AgCl.^[60,61] Subsequent linear fitting enabled the determination of C_{dl} for the NBCF electrocatalysts, employing one-half of the slope. ECSA was subsequently computed by dividing C_{dl} by the specific capacitance (C_s), equal to 0.040 mFCm^{-2} in 1 M KOH according to the literature.^[62] After that, the mass loading and ECSA of the electrocatalysts were employed for the computation of mass activity (Ag^{-1}) and specific activity (mA cm^{-2}) of the electrocatalysts respectively.

Finally, the protocols for CV and LSV tests were replicated to elucidate the ORR activity of NBCF electrocatalysts. The sole distinction lay in the range of potentials applied, spanning from 0.1 V to (-1.2) V vs. Ag/AgCl. Following this, the Tafel slopes of the electrocatalysts were deduced upon the acquisition of Tafel plots. Several LSV experiments were conducted at a scan rate of 5 mVs^{-1} within the voltage range of 0.2 to -0.8 V versus Ag/AgCl, employing different rotation speeds (400, 800, 1200, 1600, and 2000 rpm) (see Figure S2 in the Supporting Information). These experiments aimed to assess the kinetic current density and electron transfer number of NBCF electrocatalysts employing the Koutecky-Levich (K-L) equation.^[24,63]

Measurement of Zn-Air Battery Performance

In the context of ZABs, the anode was composed of a zinc foil, while the cathode was constructed through the implementation of NBCF electrocatalysts, and the electrolyte consisted of a combination of 6.0 M KOH and 0.2 M Zn(OAc)₂. The composition of the cathodes included a carbon foam acting as a gas diffusion layer, alongside NBCF electrocatalysts and a PTFE film. This air cathode facilitated the ingress of oxygen from the surrounding environment into the cell, concurrently preventing any loss of electrolyte. The power densities of the NBCF-based ZABs were determined across current densities spanning from 0 to 200 mA cm^{-2} , alongside the generation of charge and discharge polarization curves. Subsequent to a full discharge at a current density of 5 mA cm^{-2} , the capacities of the NBCF-based ZABs were calculated. Following the computation of capacities, the ZABs rate capabilities and cycling stabilities were determined by contrasting its output voltage during discharges at rates varying from 0 to 20 mA cm^{-2} , subsequently

returning to 0 mA cm^{-2} . The cycling charge-discharge performances of the NBCF-based ZABs were subsequently assessed at a constant current density of 5 mA cm^{-2} , during which both charge and discharge durations remained at 5 minutes.

Supporting Information Summary

The authors have added complementary experimental results (Linear Sweep Voltammetry at different rotation speeds, Koutecky- Levich (K-L) plots at various voltages, and Cyclic Voltammetry scans at different scan rates) in Supporting Information.

Acknowledgements

This publication has been produced benefiting from the 2232 International Fellowship for Outstanding Researchers Program of TUBITAK (Project No: 118 C330). However, the entire responsibility of the publication belongs to the owner of the publication

Conflict of Interests

The authors declare no conflict of interest.

Data Availability Statement

The data that support the findings of this study are available from the corresponding author upon reasonable request.

Keywords: Bi-functional electrocatalyst • Double perovskite oxide • Zn-air battery • B-site doping • Work function

- [1] C. Zhou, X. Chen, S. Liu, Y. Han, H. Meng, Q. Jiang, S. Zhao, F. Wei, J. Sun, T. Tan, R. Zhang, *J Am Chem Soc* **2022**, *144*, 2694.
- [2] Y. Li, M. Gong, Y. Liang, J. Feng, J.-E. Kim, H. Wang, G. Hong, B. Zhang, H. Dai, *Nat Commun* **2013**, *4*, 1805.
- [3] Y.-P. Deng, Y. Jiang, R. Liang, S.-J. Zhang, D. Luo, Y. Hu, X. Wang, J.-T. Li, A. Yu, Z. Chen, *Nat Commun* **2020**, *11*, 1952.
- [4] M. Moloudi, A. Noori, M. S. Rahamanifar, Y. Shabangoli, M. F. El-Kady, N. B. Mohamed, R. B. Kaner, M. F. Mousavi, *Adv Energy Mater* **2023**, *13*, 2203002.
- [5] T. Maiyalagan, K. A. Jarvis, S. Therese, P. J. Ferreira, A. Manthiram, *Nat Commun* **2014**, *5*, 3949.
- [6] C. C. L. McCrory, S. Jung, J. C. Peters, T. F. Jaramillo, *J Am Chem Soc* **2013**, *135*, 16977.
- [7] J. Wang, Y. Gao, D. Chen, J. Liu, Z. Zhang, Z. Shao, F. Ciucci, *ACS Catal* **2018**, *8*, 364.
- [8] S. Cherevko, S. Geiger, O. Kasian, N. Kulyk, J.-P. Grote, A. Savan, B. R. Shrestha, S. Merzlikin, B. Breitbach, A. Ludwig, K. J. J. Mayrhofer, *Catal Today* **2016**, *262*, 170.
- [9] C. Wei, R. R. Rao, J. Peng, B. Huang, I. E. L. Stephens, M. Risch, Z. J. Xu, Y. Shao-Horn, *Adv. Mater.* **2019**, *31*, 1806296.
- [10] S. Wang, A. Lu, C.-J. Zhong, *Nano Converg* **2021**, *8*, 4.
- [11] X. Wu, C. Tang, Y. Cheng, X. Min, S. P. Jiang, S. Wang, *Chem. Eur. J.* **2020**, *26*, 3906.
- [12] C. Ozgur, T. Erdil, U. Geyikci, C. Okuyucu, E. Lokcu, Y. E. Kalay, C. Toparli, *Global Challenges* **2024**, *8*, 2300199

- [13] W.-J. Yin, B. Weng, J. Ge, Q. Sun, Z. Li, Y. Yan, *Energy Environ Sci* **2019**, *12*, 442.
- [14] Y. Tong, J. Wu, P. Chen, H. Liu, W. Chu, C. Wu, Y. Xie, *J Am Chem Soc* **2018**, *140*, 11165.
- [15] M. Jiang, J. Li, Y. Zhao, L. Pan, Q. Cao, D. Wang, Y. Du, *ACS Appl Mater Interfaces* **2018**, *10*, 19746.
- [16] J. Hwang, R. R. Rao, L. Giordano, Y. Katayama, Y. Yu, Y. Shao-Horn, *Science (1979)* **2017**, *358*, 751.
- [17] D. Liu, P. Zhou, H. Bai, H. Ai, X. Du, M. Chen, D. Liu, W. F. Ip, K. H. Lo, C. T. Kwok, S. Chen, S. Wang, G. Xing, X. Wang, H. Pan, *Small* **2021**, *17*, 2101605.
- [18] A. T. Mulder, N. A. Benedek, J. M. Rondinelli, C. J. Fennie, *Adv Funct Mater* **2013**, *23*(38), 4810–4820.
- [19] J. Song, C. Wei, Z.-F. Huang, C. Liu, L. Zeng, X. Wang, Z. J. Xu, *Chem Soc Rev* **2020**, *49*, 2196.
- [20] P. Anand, M.-S. Wong, Y.-P. Fu, *J Energy Storage* **2024**, *77*, 109917.
- [21] X. Wang, H. Zhong, S. Xi, W. S. V. Lee, J. Xue, *Adv. Mater.* **2022**, *34*(50), 2107956.
- [22] Y. Zhu, L. Zhang, B. Zhao, H. Chen, X. Liu, R. Zhao, X. Wang, J. Liu, Y. Chen, M. Liu, *Adv Funct Mater* **2019**, *29*(34), 1901783.
- [23] J.-W. Zhao, Z.-X. Shi, C.-F. Li, Q. Ren, G.-R. Li, *ACS Mater Lett* **2021**, *3*, 721.
- [24] S. Yu, Z. Shui, C. Wang, Y. Lei, Y. Liu, W. Zhao, X. Chen, *J Mater Sci* **2022**, *57*, 12364.
- [25] S. Zhang, N. Wei, Z. Yao, X. Zhao, M. Du, Q. Zhou, *Int J Hydrogen Energy* **2021**, *46*, 5286.
- [26] Z. Wang, R. Lin, Y. Huo, H. Li, L. Wang, *Adv Funct Mater* **2022**, *32*, 2109503.
- [27] P. Gayen, S. Saha, K. Bhattacharyya, V. K. Ramani, *ACS Catal* **2020**, *10*, 7734.
- [28] T. Erdil, E. Lokcu, I. Yildiz, C. Okuyucu, Y. E. Kalay, C. Toparli, *ACS Omega* **2022**, *7*, 44147.
- [29] X. Cheng, E. Fabbri, M. Nachtegaal, I. E. Castelli, M. El Kazzi, R. Haumont, N. Marzari, T. J. Schmidt, *Chem. Mater.* **2015**, *27*, 7662.
- [30] X. Cao, X. Yan, L. Ke, K. Zhao, N. Yan, *ACS Appl Mater Interfaces* **2021**, *13*, 22009.
- [31] B. Zhao, L. Zhang, D. Zhen, S. Yoo, Y. Ding, D. Chen, Y. Chen, Q. Zhang, B. Doyle, X. Xiong, M. Liu, *Nat Commun* **2017**, *8*, 14586.
- [32] H. Sun, X. Xu, Y. Song, W. Zhou, Z. Shao, *Adv Funct Mater* **2021**, *31*, 2009779.
- [33] X. Xu, Y. Zhong, Z. Shao, *Trends Chem* **2019**, *1*, 410.
- [34] S. She, J. Yu, W. Tang, Y. Zhu, Y. Chen, J. Sunarso, W. Zhou, Z. Shao, *ACS Appl Mater Interfaces* **2018**, *10*, 11715.
- [35] T. Erdil, C. Toparli, *ACS Appl Energy Mater* **2023**, *6*, 11255.
- [36] X. Xu, C. Su, W. Zhou, Y. Zhu, Y. Chen, Z. Shao, *Adv. Sci.* **2016**, *3*(2), 1500187.
- [37] J. Hwang, R. R. Rao, L. Giordano, Y. Katayama, Y. Yu, Y. Shao-Horn, *Science (1979)* **2017**, *358*, 751.
- [38] J. T. Mefford, X. Rong, A. M. Abakumov, W. G. Hardin, S. Dai, A. M. Kolpak, K. P. Johnston, K. J. Stevenson, *Nat Commun* **2016**, *7*, 11053.
- [39] Y. Lv, Z. Li, Y. Yu, J. Yin, K. Song, B. Yang, L. Yuan, X. Hu, *J Alloys Compd* **2019**, *801*, 19.
- [40] N.-I. Kim, S.-H. Cho, S. H. Park, Y. J. Lee, R. A. Afzal, J. Yoo, Y.-S. Seo, Y. J. Lee, J.-Y. Park, *J Mater Chem A Mater* **2018**, *6*, 17807.
- [41] Z. Gao, L. V. Mogni, E. C. Miller, J. G. Railsback, S. A. Barnett, *Energy Environ Sci* **2016**, *9*, 1602.
- [42] R. Merkle, Y. A. Mastrikov, E. A. Kotomin, M. M. Kuklja, J. Maier, *J Electrochem Soc* **2011**, *159*, B219.
- [43] D. O. Bayraktar, E. Lökcü, C. Ozgur, T. Erdil, C. Toparli, *Int J Energy Res* **2022**, *46*, 22124.
- [44] T. Yamashita, P. Hayes, *Appl Surf Sci* **2008**, *254*, 2441.
- [45] Y. Lee, J. Suntivich, K. J. May, E. E. Perry, Y. Shao-Horn, *J Phys Chem Lett* **2012**, *3*, 399.
- [46] M. Retuerto, F. Calle-Vallejo, L. Pascual, G. Lumbeeck, M. T. Fernandez-Diaz, M. Croft, J. Gopalakrishnan, M. A. Peña, J. Hadermann, M. Greenblatt, S. Rojas, *ACS Appl Mater Interfaces* **2019**, *11*, 21454.
- [47] R. A. Rincón, J. Masa, S. Mehrpour, F. Tietz, W. Schuhmann, *Chem. Commun.* **2014**, *50*, 14760.
- [48] Y. Lee, J. Suntivich, K. J. May, E. E. Perry, Y. Shao-Horn, *J Phys Chem Lett* **2012**, *3*, 399.
- [49] D. Antipin, M. Risch, *J. Phys.: Energy* **2020**, *2*, 032003.
- [50] L. Heymann, M. L. Weber, M. Wohlgemuth, M. Risch, R. Dittmann, C. Baeumer, F. Gunkel, *ACS Appl Mater Interfaces* **2022**, *14*, 14129.
- [51] C. Alegre, E. Modica, A. S. Aricò, V. Baglio, *J. Electroanal. Chem.* **2018**, *808*, 412.
- [52] Y. Zhu, W. Zhou, J. Yu, Y. Chen, M. Liu, Z. Shao, *Chem. Mater.* **2016**, *28*, 1691.
- [53] X. Li, Y. Bai, Z. Cheng, *Adv. Sci.* **2021**, *8*(17), 2101000.
- [54] M. Qu, X. Ding, Z. Shen, M. Cui, F. E. Oropeza, G. Gorni, V. A. de la Peña O’Shea, W. Li, D.-C. Qi, K. H. L. Zhang, *Chem. Mater.* **2021**, *33*, 2062.
- [55] B. Prajapati, S. Roy, S. Sharma, A. G. Joshi, S. Chatterjee, A. K. Ghosh, *Phys. Status Solidi (b)* **2019**, *256*(5), 1800262.
- [56] R. Xie, Z. Nie, X. Hu, Y. Yu, C. Aruta, N. Yang, *ACS Appl Energy Mater* **2021**, *4*, 9057.
- [57] A. R. Zeradjanin, *ChemSusChem* **2018**, *11*, 1278.
- [58] A. R. Zeradjanin, E. Ventosa, A. S. Bondarenko, W. Schuhmann, *ChemSusChem* **2012**, *5*, 1905.
- [59] C. Wei, S. Sun, D. Mandler, X. Wang, S. Z. Qiao, Z. J. Xu, *Chem Soc Rev* **2019**, *48*, 2518.
- [60] J. Dai, Y. Zhu, Y. Zhong, J. Miao, B. Lin, W. Zhou, Z. Shao, *Adv Mater Interfaces* **2019**, *6*, 1801317.
- [61] S. Anantharaj, S. R. Ede, K. Karthick, S. Sam Sankar, K. Sangeetha, P. E. Karthik, S. Kundu, *Energy Environ Sci* **2018**, *11*, 744.
- [62] X. Ye, S. Song, L. Li, Y.-C. Chang, S. Qin, Z. Liu, Y.-C. Huang, J. Zhou, L. Zhang, C.-L. Dong, C.-W. Pao, H.-J. Lin, C.-T. Chen, Z. Hu, J.-Q. Wang, Y. Long, *Chem. Mater.* **2021**, *33*, 9295.
- [63] A. Safakas, G. Bampos, S. Bebelis, *Appl Catal B* **2019**, *244*, 225.

Manuscript received: May 8, 2024
Revised manuscript received: July 11, 2024
Accepted manuscript online: July 18, 2024
Version of record online: September 11, 2024